Available online at www.sciencedirect.com
ScienceDirect
International Journal of Heat and Mass Transfer 51 (2008) 5389–5399
International Journal of HEAT and MASS TRANSFER
www.elsevier.com/locate/ijhmt

Heat transfer correlation for hexagonal and in-line arrays of impinging jets

L.F.G. Geers [a,*], M.J. Tummers [b], T.J. Bueninck [b], K. Hanjalić [b]

[a] TNO Science and Industry - Industrial Modelling and Control, P.O. Box 155, 2600 AD Delft, The Netherlands
[b] Delft University of Technology - Faculty of Applied Sciences, P.O. Box 5046, 2600 GA Delft, The Netherlands

Received 23 April 2007; received in revised form 24 December 2007
Available online 2 May 2008

Abstract

The paper reports on the results of heat transfer measurements in hexagonal and in-line arrays of impinging jets for Reynolds numbers (based on the nozzle diameter D_m) ranging from 5×10^3 to 2×10^4. Liquid crystal thermography (LCT) was used to determine the temperature distribution on the flat impingement plate. The distance between the impingement plate and the nozzle exit plane varied between $3D_m$ and $10D_m$, while the spacing between the nozzles varied between $2D_m$ and $6D_m$. The experiments indicate that the multiple-jet heat transfer is strongly influenced by jet interactions, which, in turn, depend on the parameters mentioned above. The data set was used to construct a new correlation for the (area-averaged) Nusselt number that takes the interactions into account.

PACS: 47.27.Wg

Keywords: Heat transfer; Impinging jet; Jet array; Nusselt number correlation; Liquid crystal thermography

1. Introduction

The local heat transfer in single impinging jets has been the topic of several investigations [1–4]. For jets issuing from a plenum chamber with no turbulence, maximum heat transfer in the stagnation point has been found to coincide with the placement of the impingement surface at the end of the jet's potential core. This is generally found to be between $4D_m$ and $6D_m$ (see for instance Viskanta [5]). In the case of impinging jet arrays, Goldstein and Seol [6] proposed that this maximum would also be found at the end of the potential core, but they expected this length to be shorter due to jet-to-jet interaction prior to impingement. Such interactions are enhanced when the jets are closely spaced, and when the distance between the nozzle and the impingement plate (nozzle-to-plate distance) is relatively large. Furthermore, Goldstein and Timmers [7] show that adjacent jets interact through the ring vortices around the jet circumference, causing the shear-induced turbulence to penetrate further towards the centre of the individual jets. As a result, the stagnation point heat transfer in the multiple jet set-up is lower than in the single impinging jet. Secondly, there is an interaction due to collision of wall jets associated with the adjacent impinged jets.

As the jet-to-jet spacing (pitch) and the nozzle-to-plate distance are decreased, the fountain up-wash effect created by the collision of the wall jets becomes more pronounced. This up-wash causes flow recirculation and entrainment of spent fluid back into the central jet, thereby deteriorating heat transfer further. This was observed by San and Lai [8], who investigated the effect of jet-to-jet spacing on the heat transfer in a staggered array of confined jets at Reynolds numbers between 1×10^4 and 3×10^4. They found that the optimum heat transfer in the stagnation point was achieved for jet-to-jet spacings of approximately eight nozzle diameters.

* Corresponding author. Tel.: +31 15 269 2384; fax: +31 15 269 2111.
E-mail address: leon.geers@tno.nl (L.F.G. Geers).

0017-9310/$ - see front matter © 2008 Elsevier Ltd. All rights reserved.
doi:10.1016/j.ijheatmasstransfer.2008.01.035

Nomenclature

Roman

D_m	diameter of nozzles
H	distance between nozzles and impingement sheet or hue
I	current through impingement sheet
L	length of impingement sheet
Nu	Nusselt number, hD_m/λ
Pr	Prandtl number, $\eta c_p/\lambda$
Re	Reynolds number, $\rho v_j D_m/\eta$
T	temperature
V	voltage over impingement sheet
W	width of impingement sheet
c_p	specific heat
d	thickness
f	relative nozzle area
h	heat transfer coefficient
q	heat flux
r	radial distance to impingement point
s	pitch
v	velocity
x	coordinate along impingement plate
y	coordinate along impingement plate

Greek symbols

Γ	area averaging factor
$\alpha_{1\ldots5}$	parameters in Nusselt correlation
γ	contraction coefficient in vena contracta
δH	hue value uncertainty
δT	temperature uncertainty
ε	emission coefficient
η	dynamic viscosity
λ	conductivity
ρ	density
σ	Stefan–Boltzmann constant

Subscripts

ave	area average
c	conduction
e	electric
j	jets
r	radiation
s	surroundings

Next to the above mentioned two interactions, there is a third one that occurs in arrays of many jets. Exhaust air of the jets in the middle of the array flows outwards, forming a cross-flow for the jets on the edge of the array. For low cross-flow velocities, Barata and Durão [9] found that this gives rise to horse-shoe type vortices wrapped around the jets in the cross-flow. As a consequence, two counter-rotating vortices trail away from each impingement region. In case of strong cross-flow, impinging jets are deflected and their impingement is delayed or even prevented.

Finally, the spatial arrangement of the nozzles in the array has an important influence on the flow characteristics of multiple impinging jets. Among numerous possible spatial arrangements, the three most common ones for round nozzle arrays are staggered, in-line, and hexagonal. The number of nearest neighbours of each nozzle and the impinged area per nozzle differ per arrangement. Therefore, the arrangement of the nozzles determines the way the jets interact with each other.

The shape of the nozzles from which the jets emerge, affects the flow and consequently the heat transfer to an impingement plate. Popiel and Boguslawski [2] measured the heat transfer characteristics of jets issuing from a sharp-edged orifice and from a bell-shaped nozzle at equal Reynolds numbers. The sharp-edged orifice appeared to cause a contraction of the jet (vena contracta), that results in a higher centre-line velocity compared to the bell-shaped nozzle. As a consequence, the heat transfer in case of the sharp-edged orifice jet is higher than that in case of the bell-shaped nozzle jet, at all values of r/D_m. The differences between the local heat transfer profiles will disappear for $H/D_m > 6$ (see Colucci and Viskanta [3]).

A number of empirical correlations for the heat transfer of impinging jet arrays can be found in the literature. Goldstein and Seol [6] proposed a correlation for a single row of jets valid for $2 \leqslant H/D_m \leqslant 8$, $4 \leqslant s/D_m \leqslant 8$, and $1 \times 10^4 \leqslant Re \leqslant 4 \times 10^4$. The correlation gives the local Nusselt number as a function of the distance from the row of jets. The area-averaged Nusselt number calculated from this correlation is

$$\frac{\overline{Nu}}{Re^{0.7}} = \frac{2.9 \cdot \Gamma}{22.8 + \left(\frac{s}{D_m}\right)\left(\frac{H}{D_m}\right)^{0.5}} \tag{1}$$

in which Γ is equal to 0.908 if the area average was taken over a width of $4D_m$, $\Gamma = 0.846$ for a width of $6D_m$, and $\Gamma = 0.784$ for a width of $8D_m$.

Gardon and Cobonpue [10] conducted heat transfer measurements for in-line arrays of 5×5 and 7×7 jets emerging from round pipes. The pipes with a length of 4 inches were attached to an air supply plenum. They found a very simple relationship between the average Nusselt number and the Reynolds number, provided these dimensionless numbers were based on the pitch as the characteristic length scale and the arrival velocity as the velocity scale. The arrival velocity is defined as the velocity a jet would have in the plane of the impingement plate if the plate were not there. Using the present definition of the Reynolds and Nusselt numbers, the correlation is

$$\frac{\overline{Nu}}{Re^{0.625}} = \frac{0.933}{\left(\frac{s}{D_m}\right)^{0.375}\left(\frac{H}{D_m}\right)^{0.625}}. \quad (2)$$

This correlation was verified for $2.4 \leqslant s/D_m \leqslant 32$, $4 \leqslant H/D_m \leqslant 128$, and $4 \times 10^3 \leqslant Re \leqslant 6 \times 10^4$.

Martin [11] devised a general empirical correlation for different kinds of nozzle geometries in both in-line and hexagonal configurations valid for $2 \leqslant H/D_m \leqslant 12$, $0.004 \leqslant f \leqslant 0.04$ and $2 \times 10^3 \leqslant Re \leqslant 1 \times 10^5$

$$\frac{\overline{Nu}}{Re^{0.66}} = Pr^{0.42}\left[1 + \left(\frac{H}{D_m}\frac{\sqrt{f}}{0.6}\right)^6\right]^{-0.05} \cdot \frac{\sqrt{f} - 2.2f}{1 + 0.2\left(\frac{H}{D_m} - 6\right)\sqrt{f}}. \quad (3)$$

Here, f is the relative nozzle area defined as the ratio of the nozzle exit cross-section to the area of the square or hexagon attached to it. For the cases of the in-line and the hexagonal configurations the values of f are

$$f_{\text{inl}} = \frac{\pi}{4}\left(\frac{D_m}{s}\right)^2 \quad \text{and} \quad f_{\text{hex}} = \frac{\pi}{2\sqrt{3}}\left(\frac{D_m}{s}\right)^2. \quad (4)$$

If the jets emerge from more or less sharp edged holes instead of smooth contoured nozzles, they will contract immediately after the orifice exit. Eq. (3) can also be used in this case, provided the contracted cross-sectional area is used instead of the geometric one. This means the jet velocity v_j, the diameter of the holes D_m, and the relative nozzle area f must be replaced by the corresponding values

$$v_j' = v_j/\gamma; \quad D_m' = D_m\sqrt{\gamma}; \quad f' = f\gamma. \quad (5)$$

Here γ is the contraction coefficient, i.e. the ratio between the narrowest jet cross-section and the geometric orifice cross-section.

The above mentioned correlations all contain a term with the Reynolds number raised to a power between 0.6 and 0.7. The dependence of geometric parameters nozzle-to-plate spacing and pitch is unique for each correlation. This is due to the differences in geometry of the array and the shape of the nozzles.

This paper reports on a set of 140 heat transfer measurements in hexagonal and in-line arrays of impinging jets for Reynolds numbers ranging from 5×10^3 to 2×10^4, nozzle-to-plate spacings between $3D_m$ and $10D_m$, and pitch values between $2D_m$ and $6D_m$. For the hexagonal arrays, both sharp-edged orifices and contoured nozzle shapes were investigated. The data were used to construct a correlation that yields the area-averaged Nusselt number as a function of the Reynolds number, the nozzle-to-plate spacing, the pitch, the nozzle shape, and the geometry of the array. Details on the effect of large scale turbulent eddies in the jet array on the distribution of the Nusselt number are discussed in another paper by Geers et al. [12 and 13]. Numerical simulations of flow and heat transfer in the same jet arrays are reported by Thielen et al. [14].

2. Experiments

2.1. Wind tunnel

Well defined boundary conditions are crucial for investigating the flow of an impinging jet array. All jets in the array should have the same initial velocity profile and turbulence levels. Additionally, the jets must be swirl-free, implying a swirl-free flow upstream of the nozzle plate. A wind tunnel was constructed that met these demands. The main parts of the wind tunnel are depicted in Fig. 1.

A centrifugal fan accelerates the air which then flows through a pipe towards a rotary flow meter (Instromet, Q-75 K). The air subsequently passes through a channel with constant cross-section, a diffusing section, the settling chamber and the contraction (with area ratio 2.8) before it reaches the nozzle plate. The diffuser is equipped with five gauzes and a honeycomb to ensure that a uniform flow field approaches the nozzle plate.

The air temperature and static pressure were measured just downstream of the settling chamber by using a Pt-100 probe (S1320 series, Systemteknik AB) and a micromanometer (FC012, Furness Controls Ltd.), respectively.

2.2. Heat transfer experiments

2.2.1. Experimental rig

Fig. 2 shows the experimental rig used for impinging jet heat transfer measurements. The air issuing from a nozzle array impinges upon a stainless steel (type 304) sheet with a thickness of 25 μm. This sheet is stretched between two clamps. Two cylindrical supports bend the sheet downwards on both ends to prevent the clamps from disturbing the flow.

The impingement sheet is heated electrically by means of a current source (Delta Elektronika) that can supply up to 100 A at 4 V. The amount of electrical energy that is dissipated in the steel foil follows directly from the product of voltage drop over the impingement plate and electric current through the plate. A voltmeter (3465B, Hewlett

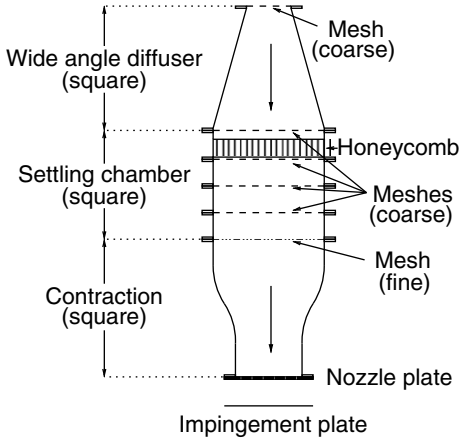

Fig. 1. Schematic drawing of the wind tunnel.

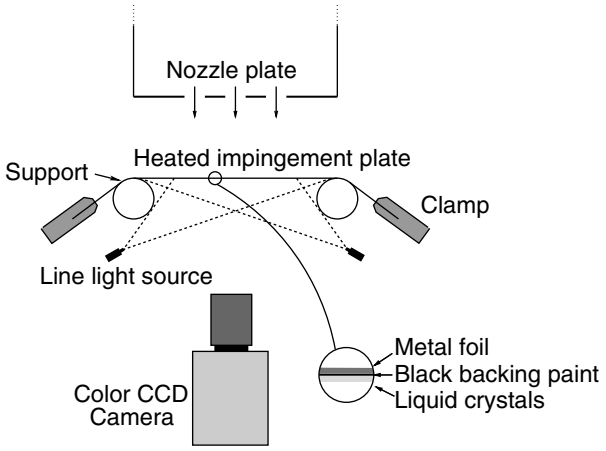

Fig. 2. Experimental rig for temperature measurements.

Packard) measures the voltage drop, while a combination of a 1 mΩ series resistance and another voltmeter (8000A, Fluke) measures the current.

The bottom side of the sheet is covered with a layer of black backing paint of about 5 μm thickness and a layer of liquid crystals (BM/R30C20W/C17-10, Hallcrest) of about 15 μm thickness to monitor the temperature of the sheet.

Four 150 W light sources (with color temperature 3200 K) were used to illuminate the liquid crystals. The light from these sources is guided through four glass fibre bundles and transferred to two 13" Light Lines (Schott-Fostec, LLC). In these devices the fibres from the bundles are arranged to produce light lines of homogeneous intensity. The infra-red radiation from the light source is reduced to a minimum by an IR-filter before the light is coupled into the fibres.

A PCO SensiCam SVGA color camera was used to acquire images of the liquid crystals. The camera is equipped with a 2/3″ CCD chip with 1280×1024 pixels that record the intensity of the incident light. The CCD chip is equipped with Bayer filters to distinguish colours.

2.2.2. Measurements

The measurements focused on the heat transfer resulting from nozzle plates with two different nozzle arrangements: in-line and hexagonal. The in-line arrangement consists of 3×3 nozzles as shown in Fig. 3a and the hexagonal arrangement consists of 13 nozzles as shown in Fig. 3b.

There were two nozzle shapes for the hexagonal arrangement, shown in Fig. 4. The sharp orifice plates have bored holes, and the contoured nozzle plates have punched holes with a contoured shape. In all cases the diameter of the nozzles D_m was 13 mm.

The three parameters that were varied in the experiments are the pitch s/D_m, the nozzle-to-plate distance H/D_m, and the Reynolds number. For all configurations (140 in total) heat transfer was measured at values of H/D_m of 3, 4, 6, 8, and 10 and Reynolds numbers of 5×10^3,10×10^3,15×10^3, and 20×10^3. For both hexagonal configurations the measurements were done at $s/D_m = 2$, 4, and 6, whereas the in-line configuration was only available with $s/D_m = 4$.

2.2.3. Data reduction

The images acquired by the camera were filtered with a median and a smoothing filter. Subsequently, they were converted from the RGB (red, green, blue) color system to the HSV (hue, saturation, intensity) color system. The hue value identifies the dominant wavelength of the light. The hue value provides a convenient way to correlate the color of liquid crystals to their temperature [15]. This was done with a lookup table resulting from the calibration procedure described below. The local values of the heat transfer coefficient h_j can be calculated from an energy balance of a small element of the impingement plate:

$$q_e = q_j + q_{r,\text{steel}} + q_{r,LC} + q_c. \tag{6}$$

On the top side of the impingement sheet heat is transferred to the environment by forced convection due to the impinging jets (q_j) and radiation ($q_{r,\text{steel}}$). Within the

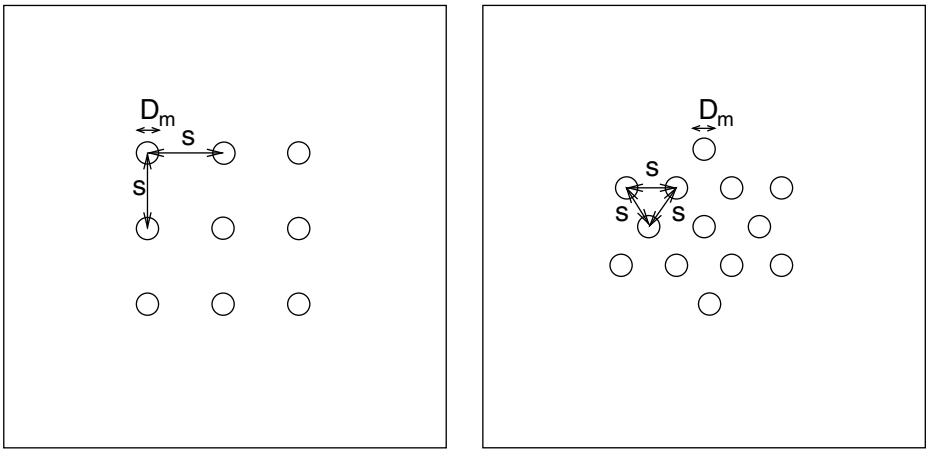

(a) in-line arrangement. (b) hexagonal arrangement.

Fig. 3. Two different nozzle arrangements for heat transfer measurements.

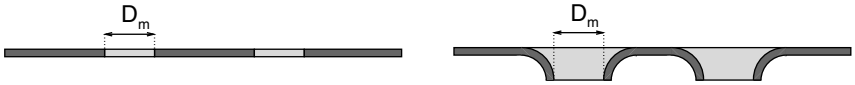

(a) sharp orifices (b) contoured nozzles

Fig. 4. Cross-sections of the two nozzle shapes.

metal sheet lateral conduction is taking place (q_c) and on the bottom side of the sheet heat is transferred to the environment by radiation ($q_{r,\mathrm{LC}}$). The sum of all the heat transfer terms is balanced by the heat production through electrical dissipation (q_e) in the metal sheet.

In Eq. (6), q_e is given by VI/(LW), where V is the voltage over the steel sheet, I is the current through the sheet, W is the width of the sheet (0.32 m), and L is the length of the sheet (0.38 m). Using the measured local sheet temperature, local values of h_j can be calculated from Eq. 6 in the form:

$$\frac{\mathrm{VI}}{\mathrm{LW}} = h_j(T - T_\mathrm{s}) + (\varepsilon_\mathrm{steel} + \varepsilon_\mathrm{LC})\sigma(T^4 - T_\mathrm{s}^4) - \lambda_\mathrm{steel} d_\mathrm{steel}\left(\frac{\partial^2 T}{\partial x^2} + \frac{\partial^2 T}{\partial y^2}\right). \quad (7)$$

Here, T is the sheet temperature, T_s is the temperature of the surroundings, $\varepsilon_\mathrm{steel}$ is the emission coefficient of the sheet (0.15), ε_LC is the emission coefficient of the paint and crystals (0.9), σ is the Stefan–Boltzmann constant ($5.67 \times 10^{-8}\,\mathrm{W\,m^{-2}\,K^{-4}}$), λ_steel is the conduction coefficient of the sheet ($16\,\mathrm{W\,m^{-1}\,K^{-1}}$), d_steel is its thickness, and x and y are the coordinates parallel to the sheet. Because the conduction term q_c is less than 1% of the total heat transfer in the element, it was not taken into account in the calculation of q_j.

The time between two consecutive images was of the order of several seconds. Because this is three orders of magnitude larger than the characteristic time scale of the flow, the images can be considered statistically independent.

The mean heat transfer was calculated from 200 images for each of the 140 different combinations of the experimental parameters. The uncertainty of h_j calculated using the method of Kline and McClintock [16] was about 2% on average, with a maximum of 9%.

2.2.4. Calibration rig and procedure

The calibration of the liquid crystals is done in the same experimental rig as the measurements to keep all external factors constant. It is especially important to keep lighting and viewing angles constant, because they strongly affect the perceived color of the crystals [17]. Water with a known temperature is recirculated on the impingement plate to impose a constant and known temperature on the crystals at which their color is recorded.

To minimize the thermal resistance, the water must be in direct contact with the impingement plate. To this end, a glass basin with an open bottom rests on silicone tubes on the steel impingement sheet. A constant temperature bath (Colora) circulates water through the basin, while the temperature is monitored using a Pt-100 probe (S1320 series, Systemteknik AB). In this way, the temperature of the water can be maintained constant within about 0.02 °C. The precision of the Pt-100 probe is 0.01 °C.

The liquid crystals were calibrated at approximately 95 points distributed over the full temperature range. Typically ten images are taken of the liquid crystals at each (constant) temperature level of the water bath. After that, all images are processed by a local median test and a smoothing filter. The median test compares the hue value of each pixel with the values of its eight direct neighbours. If this hue value is outside the 95% confidence interval calculated from its neighbours it is rejected and replaced by the median hue value of the neighbours. A 3×3 pixel moving average filter subsequently smooths the data.

All images at one temperature level are used to calculate average hue values and standard deviations of hue on each pixel position in the viewing area. Finally, arrays of these two quantities are stored in a lookup table.

2.2.5. Uncertainties in measured temperatures

The uncertainty of the temperature measurement can be determined from the uncertainty of the hue value, given by the matrix of hue standard deviations stored in the calibration file. The uncertainty of the temperature will then be

$$\delta T = \left|\frac{\mathrm{d}T}{\mathrm{d}H}\right| \delta H, \quad (8)$$

where $\mathrm{d}T/\mathrm{d}H$ is the slope of the calibration curve and δH is the uncertainty of the hue value. An example of a calibration curve is shown in Fig. 5a with horizontal error-bars representing the uncertainty of the hue. Fig. 5b shows a plot of the uncertainty of the temperature for the whole temperature range. The uncertainty is around 0.1 °C or 1% with respect to the temperature range, which is a typical value for liquid crystals according to Kasagi et al. [18].

3. Results

3.1. Local heat transfer

Contour plots of mean heat transfer results for the hexagonal array with sharp-edged orifices are presented in Fig. 6 for two values of the pitch ($s/D_m = 2$ and 6) and two nozzle-to-plate spacings ($H/D_m = 4$ and 10) at a Reynolds number of 2.0×10^4.

In the stagnation points at the impingement centre, the heat transfer is strongest in all cases considered. In between

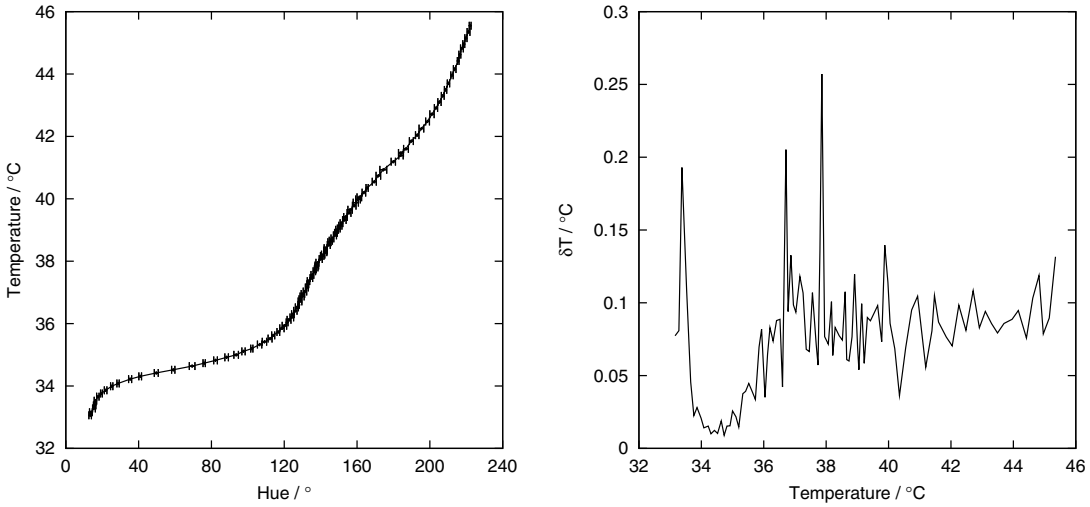

(a) Calibration with error in hue (b) Resulting error in temperature

Fig. 5. Calibration line with measurement error and the error in temperature.

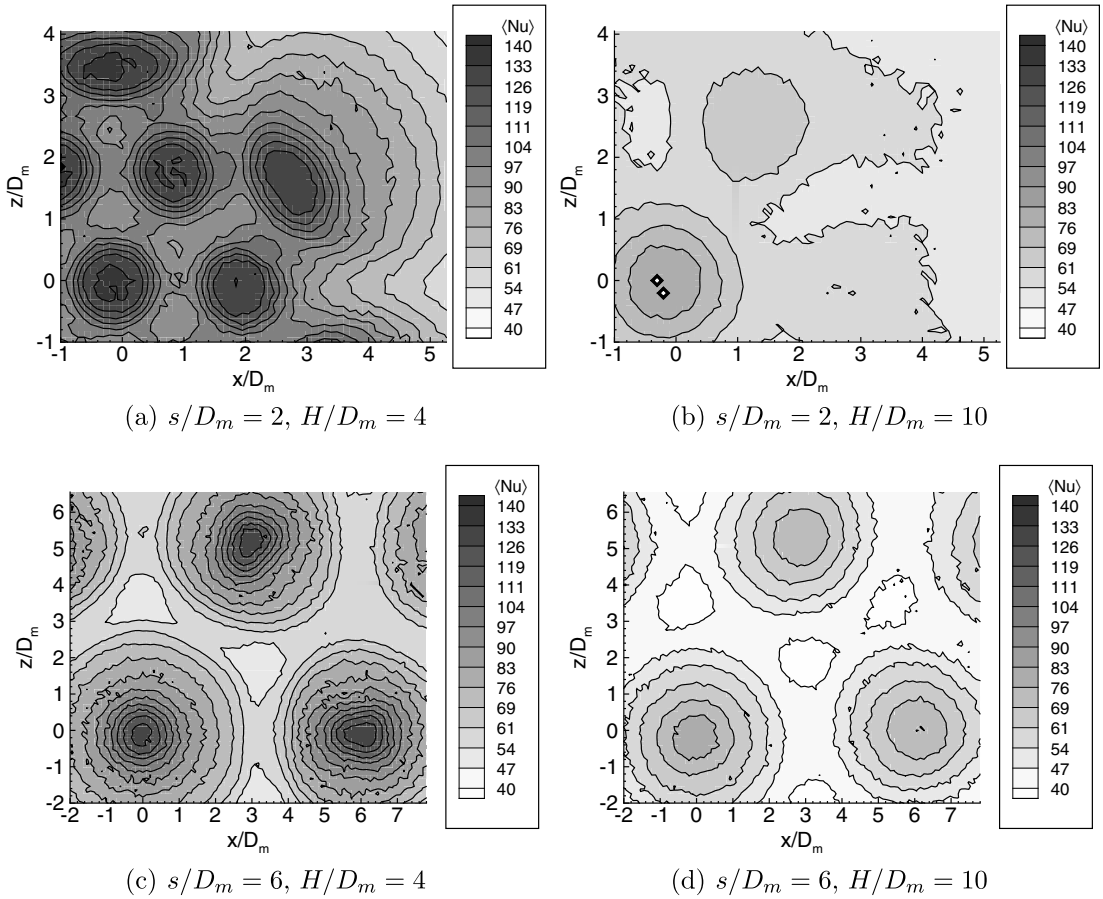

(a) $s/D_m = 2$, $H/D_m = 4$ (b) $s/D_m = 2$, $H/D_m = 10$

(c) $s/D_m = 6$, $H/D_m = 4$ (d) $s/D_m = 6$, $H/D_m = 10$

Fig. 6. Ensemble averaged Nusselt number distributions for four configurations of the hexagonal array with sharp-edged orifices at $Re = 2.0 \times 10^4$ (The two white spots near (0,0) in subfigure (b) are caused by outliers).

the impingement points the Nusselt number strongly decreases due to the decrease of the radial wall jet velocity with increasing distance from the jet impingement point and the heating of the air in the wall jet. In Fig. 6a the geometrical nozzle configuration of the jets can be clearly recognized, whereas at higher nozzle-to-plate distance this pattern appears to fade away due to the strong jet–jet interaction. At $H/D_m = 10$ the individual jets can no longer be

discerned due to spreading and mixing, dominated by the large scale structures in the shear layers enveloping the jets. In case of a larger pitch ($s/D_m = 6$, Fig. 6c and d) the distortion of the jets is weaker, and the geometrical nozzle configuration can still be discerned at $H/D_m = 10$.

The investigation of the heat transfer in the hexagonal array with contoured nozzles yielded similar results. Fig. 7 presents the ensemble averaged Nusselt number distribution for the same values of s/D_m, H/D_m, and Re as for the hexagonal array with sharp orifices shown in Fig. 6. At $H/D_m = 4$ the heat transfer in the impingement points is higher for the sharp-edged orifices than for the contoured ones. The reason for this is that the jets emerging from the sharp-edged orifices have a higher initial velocity for the same mass flow rate due to the vena contracta. In case of the contoured nozzles the vena contracta effect is much smaller or may even be absent. At $H/D_m = 10$ the differences in heat transfer are much smaller. In addition, turbulence is stronger in case of the sharp-edged orifices, which enhances the heat transfer in the impingement area.

Fig. 8 shows profiles of the Nusselt number along a line through the central jet and one of its direct neighbours as a function of H/D_m at $Re = 2.0 \times 10^4$ for both hexagonal configurations. Results are given for the sharp-edged nozzles (left) and the contoured nozzles (right) for three values of the pitch. In all cases, the Nusselt number is decreasing with increasing nozzle-to-plate distance due to the decrease of the centre-line velocity as a result of jet–jet interaction.

Fig. 8a, c, and e clearly show that the disappearance of the spatial gradients in the Nusselt number with increasing nozzle-to-plate distance is strongest for small values of the pitch, as mentioned above. Comparison of these figures with Fig. 8b, d, and f shows the effect of the nozzle shape on the heat transfer profile.

Finally, note the presence of local minima and maxima at $x/D_m \approx 2.0$ and $x/D_m \approx 4.0$ in Fig. 8f, and to a lesser extent, in Fig. 8e. These minima and maxima only occur at small nozzle-to-plate spacings, roughly for $H/D_m \leqslant 4$. Gardon and Cobonpue [10] conjectured a transition from laminar to turbulent flow to be the cause of the humps. Following this conjecture it can be stated that the laminar-turbulent transition is clearer for the contoured nozzle jets, because they have a longer potential core than the sharp orifice jets. For low nozzle-to-plate spacings the impingement plate is placed well into the potential core of the contoured nozzle jet, but it is already at, or beyond, the end of the core of the sharp-edged orifice jet. Popiel and Boguslawski [2] confirm these conclusions.

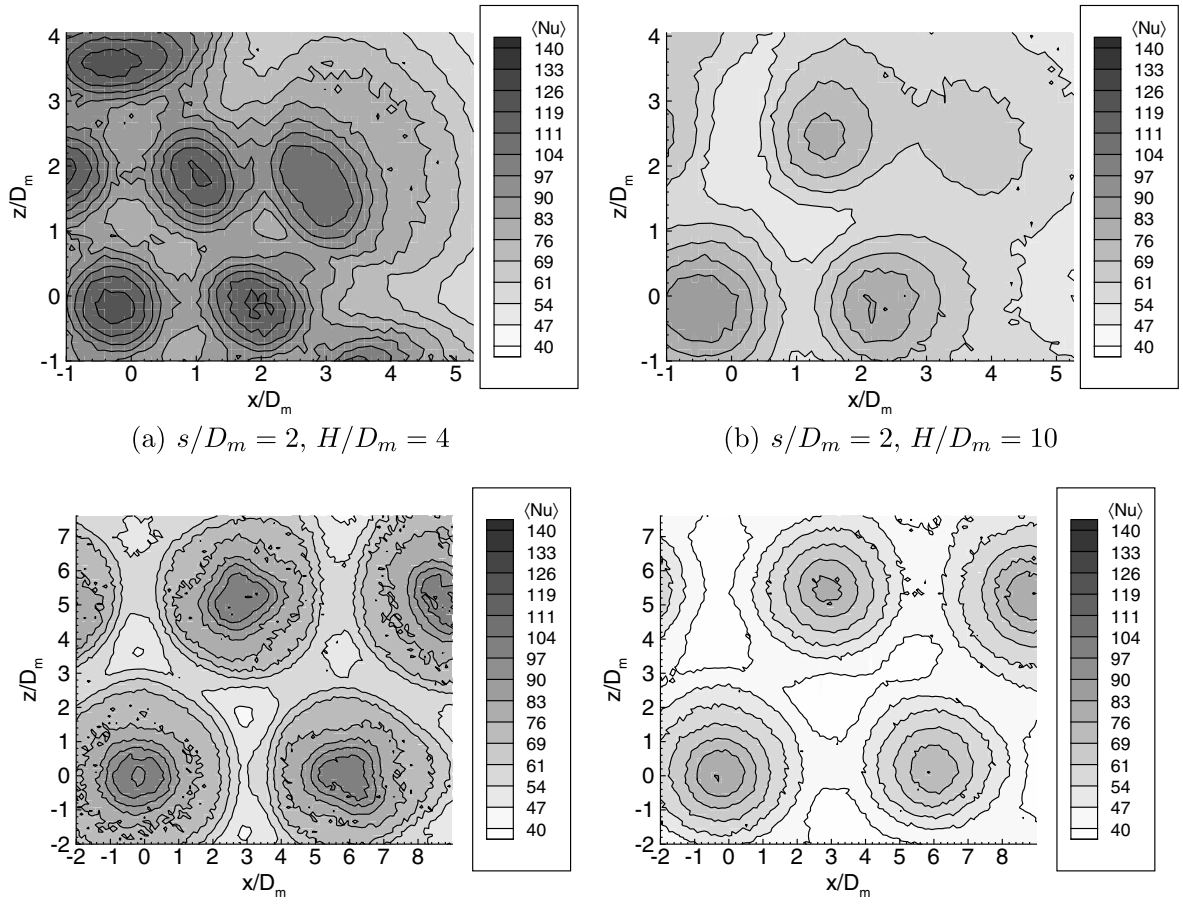

(a) $s/D_m = 2$, $H/D_m = 4$ (b) $s/D_m = 2$, $H/D_m = 10$

(c) $s/D_m = 6$, $H/D_m = 4$ (d) $s/D_m = 6$, $H/D_m = 10$

Fig. 7. Ensemble averaged Nusselt number distributions for four configurations of the hexagonal array with contoured nozzles.

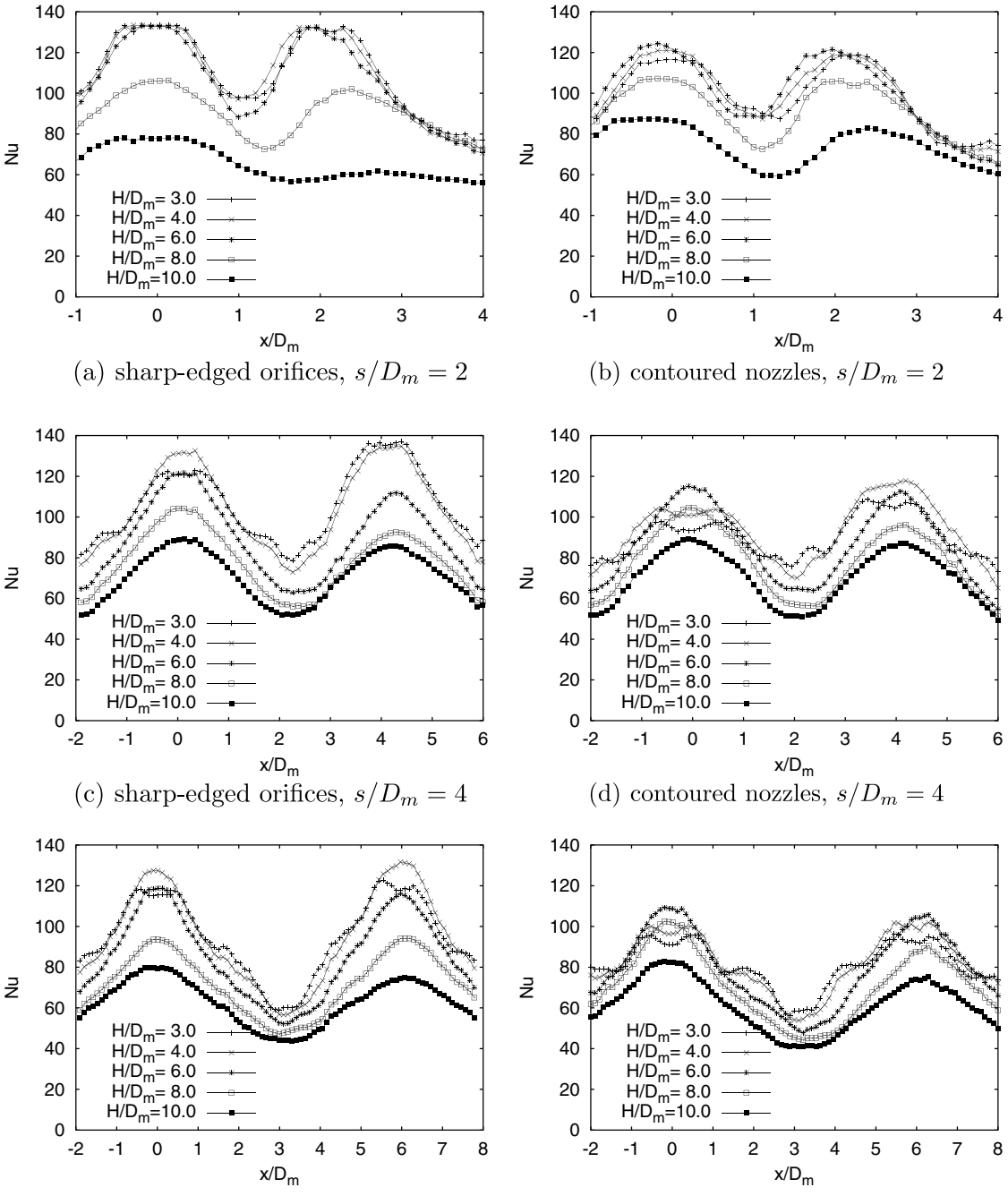

(a) sharp-edged orifices, $s/D_m = 2$ (b) contoured nozzles, $s/D_m = 2$

(c) sharp-edged orifices, $s/D_m = 4$ (d) contoured nozzles, $s/D_m = 4$

(e) sharp-edged orifices, $s/D_m = 6$ (f) contoured nozzles, $s/D_m = 6$

Fig. 8. Profiles of the local Nusselt number for all hexagonal configurations at $Re = 2.0 \times 10^4$.

3.2. Area-averaged heat transfer

The area-averaged Nusselt number was calculated for all 140 cases described above. Only a part of the total impingement plate surface is taken into account to compare average Nusselt numbers. Fig. 9 shows the regions on which average Nusselt numbers were calculated.

Goldstein and Seol [6] suggested an empirical correlation between the area-averaged Nusselt number and the Reynolds number, the pitch s/D_m and the nozzle-to-plate spacing H/D_m for a row of circular jets. We adopted their functional form to construct a new correlation to describe all data obtained in the present investigation:

$$Nu_{\text{ave}} = Re^{\alpha_1} \frac{\exp\left\{\alpha_2 \left(\frac{H}{D_m}\right)^{\alpha_3}\right\}}{\left(\frac{s}{D_m}\right)^{\alpha_4} \left(\frac{H}{D_m}\right)^{\alpha_5}}, \tag{9}$$

where α_1–α_5 are coefficients calculated from a Marquardt–Levenberg non-linear fit [19] of the equation to the experimental data in each configuration. Note also the strong resemblance with the correlation of Gardon and Cobonpue

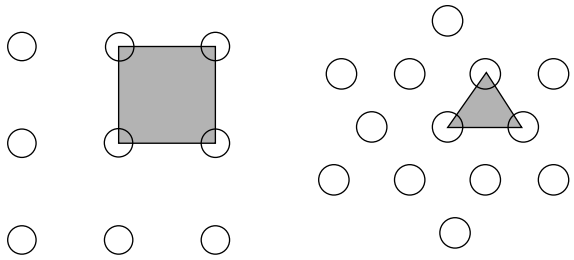

(a) In-line configuration. (b) Hexagonal configuration.

Fig. 9. Definitions of the region of interest for hexagonal and in-line nozzle plates.

Table 1
Coefficients in Eq. (9) for all configurations and the variances from the fitting procedures

Configuration shape	In-line sharp	Hexagonal sharp	Hexagonal contoured
α_1	0.58	0.64	0.67
α_2	−3.68	−3.23	−3.19
α_3	−3.00	−1.64	−1.14
α_4	n.a.	0.33	0.29
α_5	0.51	0.79	0.90
Variance	5.01	8.74	7.12

[10]. There is only an extra exponential dependence of the nozzle-to-plate spacing. Table 1 gives an overview of the values for these coefficients for all three nozzle configurations. An estimate of the variance resulting from the fitting procedures is also given. The correlation for the hexagonal configuration is valid for $5 \times 10^3 \leqslant Re \leqslant 2 \times 10^4$, $2 \leqslant s/D_m \leqslant 6$, and $3 \leqslant H/D_m \leqslant 10$. The correlation for the in-line configuration is valid in the same ranges for the Reynolds number and the nozzle-to-plate spacings, but only for $s/D_m = 4$. The values of the coefficients α_1–α_5 vary from one case to another as expected, because the correlation of Eq. 9 does not contain any information on the nozzle shape and the jet configuration. However, the differences are not large, indicating that the form of this correlation is a reasonable representation of the multiple jet heat transfer.

The resulting correlations are plotted together with the measured data in Figs. 10 and 11. For comparison also the correlations of Martin, Gardon & Cobonpue, and Goldstein & Seol were plotted, each having its own validity range. Because the correlation of Gardon and Cobonpue was derived for in-line arrays, it was not plotted for the hexagonal cases. In addition, $s/D_m = 2$ exceeded the validity ranges of both the Martin and the Goldstein & Seol correlations, so these correlations were only plotted for $s/D_m \geqslant 4$. The contraction coefficient of the jets from the sharp-edged orifices was calculated from PIV data (see Geers et al. [20]) to correctly apply Martin's correlation. An average value of $\gamma = 0.71$ was adopted here for both the hexagonal and the in-line cases. The points represent the experimental data and the lines represent the empirical correlations as presented in Eqs. (1)–(3). Each figure contains the data for each of the four Reynolds numbers investigated. For adequate comparison, the experimental data were scaled with $Re^{-\alpha 1}$.

The values of the coefficients for the Reynolds number in Eq. 9 agree well with the values found in literature. Gardon and Cobonpue [10] measured the heat transfer from in-line arrays of 5×5 and 7×7 jets issuing from a set of small pipes. They found a value of $\alpha_1 = 0.625$. Martin [11] has reported a value of 0.66 for both hexagonal and in-line sharp-edged orifice plates. Goldstein and Seol [6] investigated a row of round jets and found a value of 0.7 for α_1. However, Obot and Trabold [21], who have investigated the influence of cross-flow on the heat transfer of an in-line array of sharp-edged nozzles, presented a value of 0.8. It is unclear what the nature is of the discrepancy between this value and the Reynolds dependencies of the above mentioned correlations. The other coefficients could not be compared to values found by other researchers, because the functional forms of the correlations found were not comparable.

Comparing the correlations from literature with the present data, it appears these fit best for the contoured nozzle cases. In all cases where sharp-edged orifices were used, the correlations of Martin and Goldstein & Seol predict too low Nusselt numbers.

Although Eq. 5 was applied to correct for the vena contracta effect, there is still a discrepancy between the experimental data and Martin's correlation. It is unclear what has caused this effect.

The jet exit assembly of Goldstein and Seol [6] consists of steel delivery tubes with orifices. The diameter ratio of the orifices and the delivery tubes is about 0.4. Additionally, the orifices have a length-to-diameter ratio of 1. In the present configuration the diameter ratio of the orifices to the wind tunnel exit is about 0.04, a factor 10 smaller. The length-to-diameter ratio of the orifices is 0.15, a factor 6 smaller. These geometric differences strongly affect the contraction of the jets, hence causing a different jet flow compared to the flat sharp edged orifices used here.

The discrepancy between the experimental data and the correlations from literature is largest for the in-line geometry. On the other hand, the Gardon & Cobonpue correlation adequately fits the data for the in-line geometry, despite the fact that their jets were produced by 4 inch long pipes.

The coefficient α_4 for the hexagonal sharp-edged orifice plate is slightly higher than for the contoured nozzle plate. This means that the Nusselt number decreases faster with increasing pitch for the sharp-edged orifice plate. As was shown earlier, the sharp-edged orifice jets produce more turbulence that causes spent air of the cente jets to mix with fresh air from the neighbouring jets. This causes the strongly decreasing Nusselt number values in the impingement zones of the neighbouring jets, which in turn affects the area-averaged Nusselt numbers.

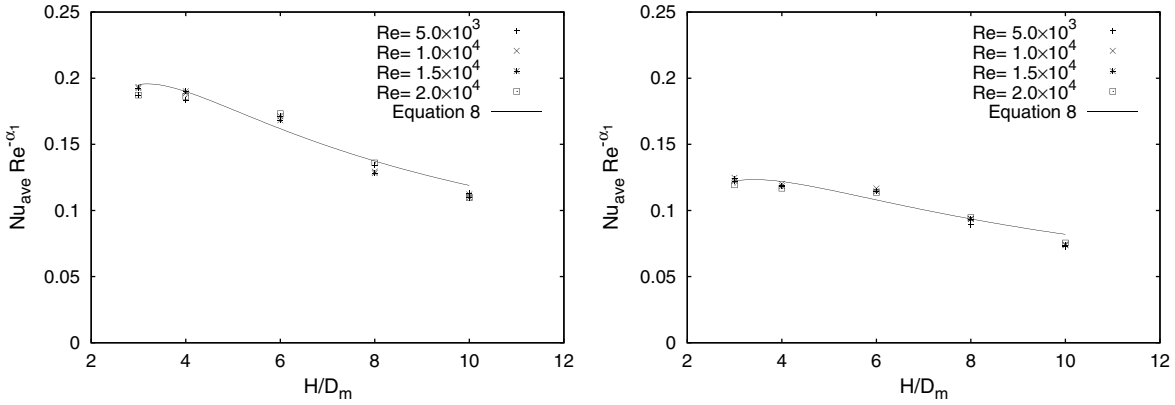

(a) sharp-edged orifices, $s/D_m = 2$ (b) contoured nozzles, $s/D_m = 2$

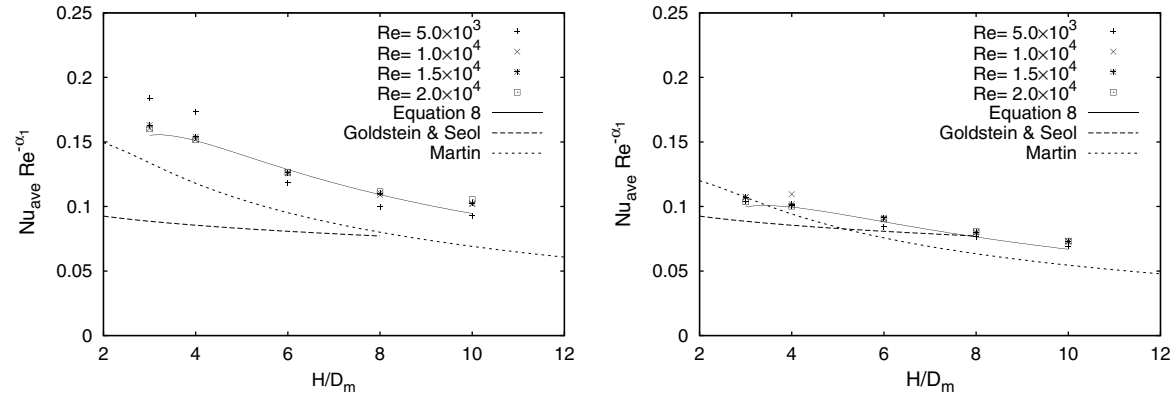

(c) sharp-edged orifices, $s/D_m = 4$ (d) contoured nozzles, $s/D_m = 4$

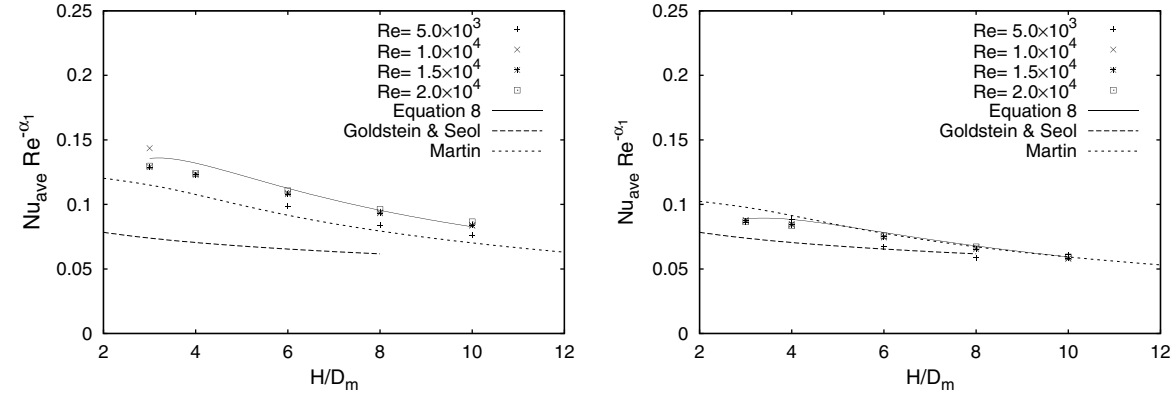

(e) sharp-edged orifices, $s/D_m = 6$ (f) contoured nozzles, $s/D_m = 6$

Fig. 10. Experimental data and correlations plotted for the hexagonal configurations.

For the hexagonal configuration with sharp-edged orifices the mean Nusselt numbers do not vary much with H/D_m for $H/D_m \leqslant 4$, similar to the Nusselt number profiles shown in Fig. 8. Above $H/D_m = 4$ the Nusselt number decreases with increasing H/D_m. The effect is strongest for $s/D_m = 2$. The same trend can be seen in the data of the hexagonal configuration with contoured nozzles, except, the decrease of the Nusselt number sets in as $H/D_m > 6$. Again this is clearest for $s/D_m = 2$. This effect can be attributed to the potential core length of the jets.

4. Conclusions

Liquid crystal measurements of surface heat transfer have been performed in impinging jet arrays with two different orifice configurations and two nozzle shapes to study the effect of various parameters on the heat transfer.

Distributions of the Nusselt number over the impingement plate show that the heat transfer is strongest in the impingement points. In between the impingement points the Nusselt number decreases due to the decrease of radial

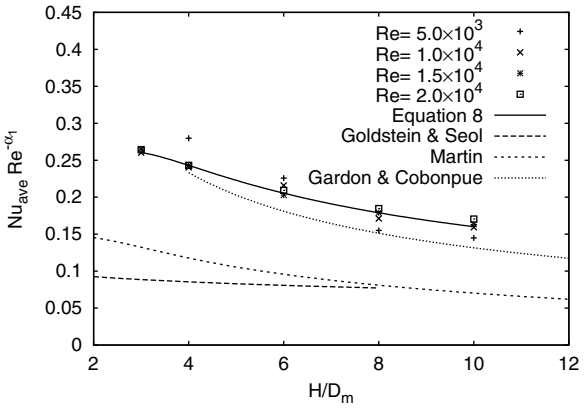

Fig. 11. Experimental data and correlations plotted for the in-line configuration.

wall jet velocity and heating of the air in the wall jet with increasing distance from the impingement point. The geometrical nozzle configuration can be clearly recognized at low nozzle-to-plate spacings. With increasing nozzle-to-plate spacing the pattern fades out due to jet–jet interaction, which is particularly strong at low values of the pitch.

Sharp edged orifice jets display a vena contracta effect that is much less pronounced or even absent for contoured nozzle jets. Thus, for the same Reynolds number, sharp edged orifice jets effectively have a higher initial core velocity resulting in higher impingement point heat transfer. Additionally, shear layer turbulence is stronger in the case of sharp edged orifice jets. This effect is clearest for low values of the nozzle-to-plate spacing. At nozzle-to-plate spacings exceeding the length of the potential core of the jets (typically $H/D_m \leqslant 4$), the difference in impingement point heat transfer diminishes.

A non-dimensional correlation between the area-averaged Nusselt number, the jet Reynolds number, the pitch, and the nozzle-to-plate spacing was found that satisfactorily fitted the experimental data. The coefficients vary for different nozzle shapes and configurations, because the correlation does not contain parameters quantifying these aspects.

Acknowledgement

This work was sponsored by the Dutch Technology Foundation STW of the Netherlands, TNO, and Rademaker-Den Boer.

References

[1] J.W. Baughn, S. Shimizu, Heat transfer measurements from a surface with uniform heat flux and an impinging jet, Trans. ASME - J. Heat Transfer 111 (1989) 1096–1098.

[2] C.O. Popiel, L. Boguslawski, Mass or heat transfer in impinging single, round jets emitted by a bell-shaped nozzle and sharp-ended orifice, in: Heat Transfer 1986, Proceedings of 8th International Heat Transfer Conference, vol. 3, 1986, pp. 1187–1192.

[3] D.W. Colucci, R. Viskanta, Effect of nozzle geometry on local convective heat transfer to a confined impinging air jet, Exp. Therm. Fluid Sci. 13 (1996) 71–80.

[4] J. Lee, S.-J. Lee, The effect of nozzle configuration on stagnation region heat transfer enhancement of axisymmetric jet impingement, Int. J. Heat Mass Transfer 43 (2000) 3497–3509.

[5] R. Viskanta, Heat transfer to impinging isothermal gas and flame jets, Exp. Therm. Fluid Sci. 6 (1993) 111–134.

[6] R.J. Goldstein, W.S. Seol, Heat transfer to a row of impinging circular air jets including the effect of entrainment, Int. J. Heat Mass Transfer 34 (8) (1991) 2133–2147.

[7] R.J. Goldstein, J.F. Timmers, Visualization of heat transfer from arrays of impinging jets, Int. J. Heat Mass Transfer 25 (12) (1982) 1857–1868.

[8] J. San, M. Lai, Optimum jet-to-jet spacing of heat transfer for staggered arrays of impinging jets, Int. J. Heat Mass Transfer 44 (2001) 3997–4007.

[9] J.M.M. Barata, D.F.G. Durão, Laser-doppler measurements of impinging jet flows through a crossflow, in: Proceedings of the 11th International Symposium on Applications of Laser Techniques to Fluid Mechanics, Lisbon, 2002.

[10] R. Gardon, J. Cobonpue, Heat transfer between a flat plate and jets of air impinging on it, Int. Dev. Heat Trans., ASME, New York, 1962, pp. 454–460.

[11] H. Martin, Advances in Heat Transfer, vol. 13, Academic Press, 1977, pp. 1–60.

[12] L.F.G. Geers, M.J. Tummers, K. Hanjalić, PIV-based identification of turbulent structures in normally impinging multiple jets, Phys. Fluids 17 (2005) 055105.

[13] L.F.G. Geers, K. Hanjalić, M.J. Tummers, Wall imprint of turbulent structures and heat transfer in multiple impinging jet arrays, J. Fluid Mech. 546 (2006) 255–284.

[14] L. Thielen, K. Hanjalic, H. Jonker, R. Manceau, Predictions of flow and heat transfer in multiple impinging jets with an elliptic-blending second-moment closure, Int. J. Heat Mass Transfer 48 (8) (2005) 1583–1598.

[15] J.L. Hay, D.K. Hollingsworth, A comparison of trichromic systems for use in the calibration of polymer-dispersed thermochromic liquid crystals, Exp. Therm. Fluid Sci. 12 (1996) 1–12.

[16] S.J. Kline, F.A. McClintock, Describing uncertainties in single-sample experiments, Mech. Eng. 75 (1953) 3–8.

[17] M.R. Anderson, Thermochromic liquid crystal thermography: hysteresis, illumination and imaging system effects, image processing and applications, Ph.D. Thesis, University of California at Davis, Davis (CA), 1999.

[18] N. Kasagi, R.J. Moffat, M. Hirata, Handbook of Flow Visualisation, second ed., Taylor & Francis, New York, 2001 (Chapter 8).

[19] W.H. Press, S.A. Teukolsky, W.T. Vetterling, B.P. Flannery, Numerical Recipes in C – The art of Scientific Computing, second ed., Cambridge University Press, Cambridge, 1992.

[20] L.F.G. Geers, M.J. Tummers, K. Hanjalić, Experimental investigation of impinging jet arrays, Exp. Fluids 36 (2004) 946–958.

[21] N.T. Obot, T.A. Trabold, Impingement heat transfer within arrays of circular jets: Part 1 – effects of minimum, intermediate, and complete crossflow for small and large spacings, Trans. ASME - J. Heat Transfer 109 (1987) 872–879.